Switching Loss Reduction for an MMC-Fed AC/DC Converter

KAVEH POURESMAEIL (Graduate Student Member, IEEE), **MAURICE G.L. ROES** (Member, IEEE), **NICO H. BAARS, AND CORNELIS G.E. WIJNANDS**

Department of Electrical Engineering, Eindhoven University of Technology, 5600MB Eindhoven, The Netherlands

CORRESPONDING AUTHOR: KAVEH POURESMAEIL (e-mail: k.pouresmaeil@tue.nl).

ABSTRACT Medium-voltage connected ultra-fast chargers are getting more popular for charging electric vehicles with large battery capacities. Here, the solution based on a modular multilevel converter is more promising, since the isolation stage can be realized as a single medium-frequency transformer interconnecting the modular multilevel converter to a single-phase ac/dc converter. A new operating scheme is proposed for this converter, enabling zero-voltage switching and nearly zero-current switching across the entire load range. In contrast to the conventional phase-shift control method, the proposed scheme effectively reduces the reactive power through the ac/dc converter, leading to decreased turn-off switching losses in the ac/dc converter and a lower RMS current stress in the power path. A control scheme, integrating the operating principle, is developed for the modular multilevel converter. The method is verified through simulation and measurements on a scaled-down prototype. The results validate the theoretical analysis and practical feasibility of the proposed operating principle and the developed control scheme.

INDEX TERMS Charging infrastructure for EVs, grid-connected converters, modular multi level converters, ac/dc converter, isolated, bi-directional, soft-switching.

I. INTRODUCTION

Medium-Voltage (MV) connected ultrafast chargers are indispensable for charging EVs with a large battery capacity, such as electric trucks and ships. Conventional solutions consist of a low-voltage ac/dc converter connected to the MV grid by means of a Low-Frequency (LF) step-down transformer. A notable reduction in system size can be achieved by increasing the operating frequency of the transformer [1]. This, however, requires a MV-connected converter to interface the MV-grid to a Medium-Frequency Transformer (MFT). In this regard, solutions based on Modular Multilevel Converters (MMC) are gaining more attention mainly because of the scalability and the added functionality (e.g. grid support) and power density [2]. Fig. 1 shows an ac/ac-MMC-based ultrafast charger, where the MMC converts the grid voltage to a MF AC voltage [3], [4]. The MFT is used to isolate and step down the MMC voltage to a suitable voltage level for EV charging. Finally, the Low-Voltage Converter (LVC) is responsible for the conversion to a dc output voltage. One of the advantages of such a configuration is that the voltage
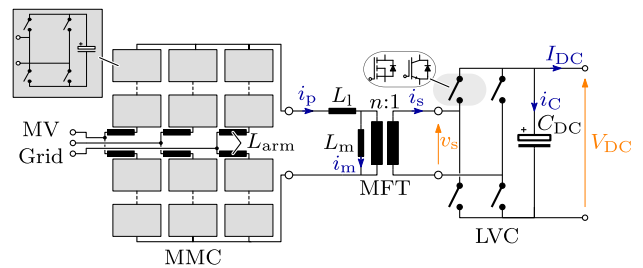

FIGURE 1. Circuit configuration of an ac/ac-MMC-based ultra-fast charger.

and current waveforms supplied to the transformer can be chosen freely and used to optimize the performance. Typical choices would be a sinusoidal or rectangular voltage waveform. However, due to the inherent power fluctuation of single-phase systems operating with a sinusoidal waveform, a rectangular waveform is preferred to transfer the power [5].

Vehicle-to-grid operation requires bi-directional power flow control. Conventionally, this is achieved in MMC-fed

converters by means of phase-shift control [6], [7], [8]. In this method, the transferred power is controlled by the phase-shift angle between the ac-terminal voltages of the MMC and LVC. Nonetheless, similar to conventional dual active bridge converters, phase-shift control leads to a limited region of soft switching operation and a considerable amount of reactive power, which causes large switching losses during turn-off transitions, and excessive conduction losses in the power path [9].

In typical phase-shift-controlled converters, both the active and reactive components of the transferred power are a function of the phase-shift angle. In MMC-fed ac/dc converters, on the other hand, the active and reactive powers can be controlled independently, due to the multilevel voltage output that the MMC can generate. To do so, the MMC acts as a controlled voltage source whose interaction with the ac-terminal voltage v_s of the LVC, the arm inductance L_{arm}, and the leakage inductance L_l of the MFT shapes the current through the MFT. In [10], closed-loop current control is presented for an MMC-based HVdc-MVdc system, resulting in sinusoidal currents through the MFT and lossless switching in the ac/dc converter. However, this method leads to a large amount of pulsating power and low current utilization of components. The current is not limited to sinusoidal waveforms, but can have any other shape. In [11], a current control method is introduced that achieves a purely active trapezoidal current through the MMC-fed LVC, and therefore high current utilization of the components. Since this current lacks a reactive component, it does not provide the commutation current necessary for Zero-Voltage Switching (ZVS) of the power switches. Consequently, only Zero-Current Switching (ZCS) can be realized, resulting in switching losses during the turn-on transitions of power switches, attributed to the switch-node capacitance. This can also lead to an impaired electromagnetic interference performance.

The authors have first proposed the Pulse Amplitude Control (PAC) method for MMC-based converters and studied its advantages over the conventional methods in [4]. In this method, the MMC output voltage is built up out of three pulse-shaped voltage components, producing a trapezoidal current with an adjustable reactive component through the LVC. This results in ZVS and nearly-ZCS operation of the power switches and minimizes the RMS current and therefore conduction losses. Due to the trapezoidal current, the proposed method yields a high current utilization of the MFT and LVC. In this paper, a dedicated control scheme that addresses the proposed operating principle and the stable operation of the MMC is developed and discussed in detail. Simulation results are provided for an MMC-based charger. Furthermore, experimental validations of the MMC-based charger converter is done using a scaled-down laboratory prototype. These simulations and experimental measurements confirm the performance and functionality of the proposed operating principle and developed control scheme for the MMC-based charger.
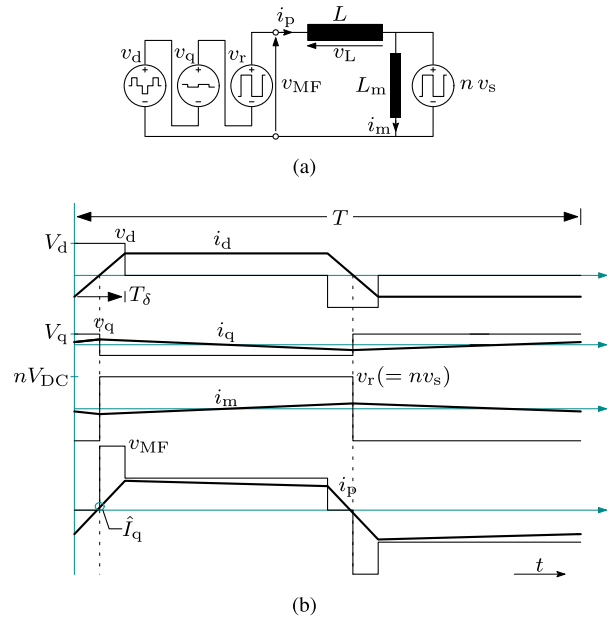

FIGURE 2. (a) Simplified representation of the MMC-connected LVC applying PAC, (b) ac-terminal voltages and the resulting current through the equivalent inductance L and magnetizing inductance L_m of the MFT.

II. PROPOSED OPERATING PRINCIPLE

Fig. 2 represents the interconnection of the MMC and the LVC and the voltage and current waveforms of the converter using the proposed method. Applying the PAC method, the LVC switches with a constant duty cycle of 50%, thereby producing a rectangular voltage across its ac terminals. The MMC produces a voltage v_{MF} comprised of the primary referred of the rectangular voltage $v_r = n\,v_s$ and two other pulse voltages. The first component v_d is a pulse waveform with a pulse width of $T_\delta = \delta/2\pi f_s$, amplitude V_d, and phase shift $\pi/2$ with regard to v_s. The series inductance L is composed of two third of the arm inductance L_{arm}, the primary-referred leakage inductance of the transformer L_l, and the external series inductance L_s, if any are added. Since the MMC and the LVC are connected through the inductance L, the resulting trapezoidal current i_d through the MFT is phase aligned with v_s. Its amplitude is

$$\hat{I}_d = \frac{V_d\,\delta}{4\pi f_s L}. \tag{1}$$

Averaging $n\,v_s \cdot i_d$ over the switching period gives the output power

$$P_{MF} = \frac{1}{T}\int_0^T n\,v_s \cdot i_d\,dt$$
$$= \frac{V_d\,n\,V_{DC}}{4\pi f_s L}\frac{\delta}{\pi}\left(\pi - \frac{\delta}{2}\right). \tag{2}$$

The transferred power can be adjusted by changing V_d and/or δ. The second voltage component v_q is a square waveform with an amplitude V_q and phase shift π with regard to v_s so as to produce a purely reactive current i_q through the MFT. The

amplitude of the resulting reactive current

$$\hat{I}_q = \frac{V_q}{4 f_s L} \tag{3}$$

can be adjusted by changing V_q. In addition to the MMC, the magnetizing inductance of the MFT introduces a reactive current component. As can be seen from Fig. 2(a), the magnetizing current will have a triangular waveform with peak amplitude equal to

$$\hat{I}_m = \frac{n V_{DC}}{4 f_s L_m}, \tag{4}$$

where L_m represent the magnetizing inductance of the MFT. The switching current I_{sw} of the power devices is determined by the total reactive current delivered to the LVC by both the currents i_q and i_m and, using (3) and (4), is found to be

$$I_{sw} = n \left(\hat{I}_q + \hat{I}_m \right) = \frac{1}{4 f_s} \left(\frac{n V_q}{L} + \frac{n^2 V_{DC}}{L_m} \right). \tag{5}$$

The first term of (5) is adjustable through the voltage component v_q of the MMC voltage v_{MF} to change the switching current at the LVC. As a prominent advantage, the switching current can be set to the minimum commutation current required to charge or discharge the switch-node capacitance and maintain ZVS operation of the LVC. As a result, the switching current should fulfill

$$I_{sw} \geq \frac{C V_{DC}}{t_d}, \tag{6}$$

where C and t_d represent the switch-node capacitance and the dead time in each leg of the LVC [12]. Unlike the phase-shift control method, the current of the bridge is switched off at a very low value when applying the PAC method. Therefore, by minimizing the switching current I_{sw}, all the power switches of the LVC experience ZVS and nearly ZCS over the full load range.

III. CONTROL OF THE MMC
A. GENERAL CONTROL APPROACH

In the MMC, each arm consists of a series connection of several sub-modules, whose ac-link voltages are a function of their dc-link voltages and switching functions. Hence, each sub-module, and therefore the aggregate of all sub-modules in one arm of the MMC can be modeled by a controlled voltage source, as shown in Fig. 3. Common-mode (Σ) and differential-mode (Δ) components of the arm voltages and currents can be defined as

$$\begin{cases} v_y^\Sigma = \frac{v_y^u + v_y^l}{2} \\ i_y^\Sigma = \frac{i_y^u + i_y^l}{2} \\ v_y^\Delta = \frac{v_y^u - v_y^l}{2} \\ i_y^\Delta = \frac{i_y^u - i_y^l}{2} \end{cases} \text{, where } y \in \{a, b, c\} \tag{7}$$

Analyzing the leg current and voltage components illustrates that the MMC and LV grid interact through the differential-mode components. On the other hand, the interaction between
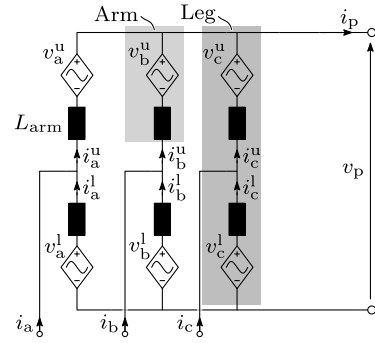

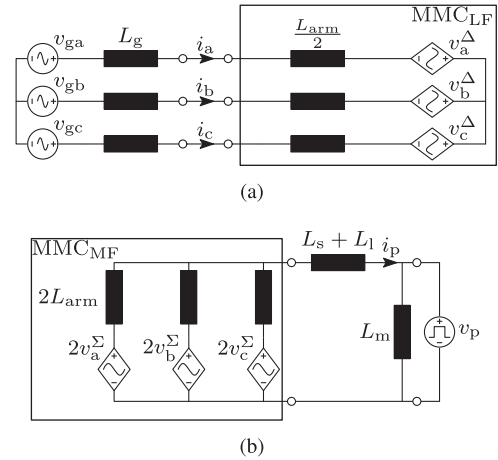**FIGURE 3. Equivalent circuit of the ac/ac MMC.**

FIGURE 4. (a) LF-terminal model of the MMC (b) MF-terminal model of the MMC.
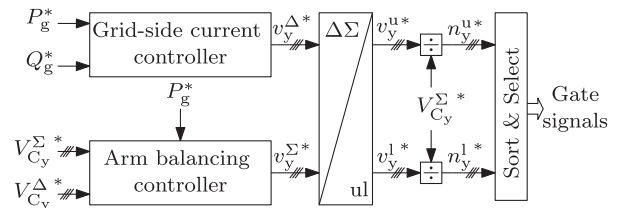

FIGURE 5. General control scheme of the MMC.

the MMC and MF side is governed by the common-mode components [3]. As a result, two terminal models can be defined for the MMC as shown in Fig. 4.

For the MMC to function stably, it is crucial to implement an appropriate control strategy for its terminal variables. The mismatch between the average power of the input and output ports of the MMC should be controlled to the power losses of the MMC, otherwise it will disturb the total energy balance within the MMC [13]. As a result, the implementation of the MMC requires a control algorithm to regulate the input and output terminal powers, thereby ensuring the total energy balance within the MMC as shown in Fig. 5. In this context, V_{Cy}^Σ corresponds to the total energy stored in the sub-module

capacitances of an MMC leg, while $V_{C_y}^{\Delta}$ is related to the energy discrepancy between the upper arm and its corresponding lower arm. These variables are expressed as follows

$$V_{C_y}^{\Sigma} = \frac{V_{C_y}^u + V_{C_y}^l}{2} \tag{8}$$

$$V_{C_y}^{\Delta} = \frac{V_{C_y}^u - V_{C_y}^l}{2} \tag{9}$$

where $V_{C_y}^u$ and $V_{C_y}^l$ are sum of the sub-module capacitor voltages in the upper and its corresponding lower arm, respectively. The grid-side current controller regulates the active and reactive power exchanged with the grid, and the arm balancing controller ensures total energy balance, as well as an equal energy distribution among the MMC arms. Here, circulating currents between legs are intentionally generated to exchange energy between arms and legs and reach an equal distribution of energy across all of them. The circulating currents are generated as common-mode components, since the grid-side terminal variables (differential-mode components) are supposed to be balanced and with the lowest harmonic content as possible. To this end, the common-mode voltage of the arm can be expressed as

$$v_y^{\Sigma} = v_{0_y}^{\Sigma} + v_{\odot_y}^{\Sigma}, \tag{10}$$

where $v_{0_y}^{\Sigma}$ is meant to regulate the total energy of the MMC and, therefore, is the same for all three legs. $v_{\odot_y}^{\Sigma}$, however, is supposed to regulate the energy difference between the arms by generating circulating currents and its value may differ among the three legs [13]. It is noteworthy that the grid-side current controller is similar to that of grid-connected voltage source converters. Since the integration of the PAC method does not involve any alteration in this controller, it will not be studied here, and the detailed discussion can be found in [3]. On the other hand, with the aim of integration of the PAC method in the MMC control, the analysis of the MMC (internal and total) energy will be provided. The dynamic of the arm energy follows from [13]

$$\frac{dW_y^u}{dt} = v_y^u i_y^u = \left(v_y^{\Sigma} + v_y^{\Delta}\right)\left(i_y^{\Sigma} + i_y^{\Delta}\right) \tag{11}$$

$$\frac{dW_y^l}{dt} = v_y^l i_y^l = \left(v_y^{\Sigma} - v_y^{\Delta}\right)\left(i_y^{\Sigma} - i_y^{\Delta}\right) \tag{12}$$

The differential- and common-mode components of the arm energy can be defined as follows

$$W_y^{\Sigma} = \frac{W_y^u + W_y^l}{2} \tag{13}$$

$$W_y^{\Delta} = \frac{W_y^u - W_y^l}{2} \tag{14}$$

Differentiation of W_y^{Σ} and W_y^{Δ} using (11) and (12) gives

$$\frac{dW_y^{\Sigma}}{dt} = v_y^{\Sigma} i_y^{\Sigma} + i_y^{\Delta} v_y^{\Delta} \tag{15}$$

$$\frac{dW_y^{\Delta}}{dt} = v_y^{\Sigma} i_y^{\Delta} + v_y^{\Delta} i_y^{\Sigma} \tag{16}$$

These equations illustrate the set of the variables that can be altered to adjust the total energy of a leg and the energy difference between upper and lower arms. Using (10) and substituting (13) and (14) into (15) and (16) provides

$$\frac{dW_y^{\Sigma}}{dt} = \frac{1}{2}i_y v_y^{\Delta} + v_{0_y}^{\Sigma}\frac{i_p}{3} + v_{\odot_y}^{\Sigma}\frac{i_p}{3} + v_{0_y}^{\Sigma}i_{\odot_y}^{\Sigma} + v_{\odot_y}^{\Sigma}i_{\odot_y}^{\Sigma} \tag{17}$$

$$\frac{dW_y^{\Delta}}{dt} = \frac{1}{2}i_y v_{0_y}^{\Sigma} + v_y^{\Delta}\frac{i_p}{3} + \frac{1}{2}i_y v_{\odot_y}^{\Sigma} + v_y^{\Delta}i_{\odot_y}^{\Sigma} \tag{18}$$

where i_y, i_p, and $i_{\odot_y}^{\Sigma}$ represent the grid phase current, the primary winding current of the MFT, and the circulating current of leg y. Averaging (17) and (18) over one grid cycle in steady state, given the fact that the circulating voltage component and corresponding current component are 90° out of phase (due to the arm inductance), gives

$$\frac{d\overline{W_y^{\Sigma}}}{dt} = \overline{\frac{1}{2}i_y v_y^{\Delta}} + \overline{v_{0_y}^{\Sigma}\frac{i_p}{3}} + \overline{v_{\odot_y}^{\Sigma}\frac{i_p}{3}} + \overline{v_{0_y}^{\Sigma}i_{\odot_y}^{\Sigma}} \tag{19}$$

$$\frac{d\overline{W_y^{\Delta}}}{dt} = \overline{\frac{1}{2}i_y v_{0_y}^{\Sigma}} + \overline{v_y^{\Delta}\frac{i_p}{3}} + \overline{\frac{1}{2}i_y v_{\odot_y}^{\Sigma}} + \overline{v_y^{\Delta}i_{\odot_y}^{\Sigma}} \tag{20}$$

The sum of the first two terms of (19) are supposed to be zero in steady state, since it is proportional to the sum of the power going to the grid and to the MFT. In other words, these terms are controlling the power flow through the MMC and cannot be used for internal energy balancing. Assuming different frequencies for the grid and MFT voltages, the first two terms of (20) are zero. This provides one with

$$\frac{d\overline{W_y^{\Sigma}}}{dt} = \overline{v_{\odot}^{\Sigma}\frac{i_p}{3}} + \overline{v_{0_y}^{\Sigma}i_{\odot_y}^{\Sigma}} \tag{21}$$

$$\frac{d\overline{W_y^{\Delta}}}{dt} = \overline{\frac{1}{2}i_y v_{\odot_y}^{\Sigma}} + \overline{v^{\Delta}i_{\odot_y}^{\Sigma}} \tag{22}$$

In order for W_y^{Σ} and W_y^{Δ} to be controllable, $v_{\odot_y}^{\Sigma}$ must include MF and LF components. Therefore, $v_{\odot_y}^{\Sigma}$ is composed of

$$v_{\odot_y}^{\Sigma} = \overbrace{v_{\odot,1_y}^{\Sigma}}^{\text{LF}} + \overbrace{v_{\odot,2_y}^{\Sigma}}^{\text{MF}} \tag{23}$$

Substitution of (23) into (21) and (22) and then ignoring oscillatory terms when averaging gives

$$\frac{d\overline{W_y^{\Sigma}}}{dt} = \overline{v_{\odot,2_y}^{\Sigma}\frac{i_p}{3}} + \overline{v_{0_y}^{\Sigma}i_{\odot,2_y}^{\Sigma}} \tag{24}$$

$$\frac{d\overline{W_y^{\Delta}}}{dt} = \overline{\frac{1}{2}i_y v_{\odot,1_y}^{\Sigma}} + \overline{v^{\Delta}i_{\odot,1_y}^{\Sigma}} \tag{25}$$

From the last two equations, it can be concluded that the total energy mismatch between the legs can be controlled by adjusting $v_{\odot,2_y}^{\Sigma}$, and the energy mismatch between the upper and lower arms can be corrected using $v_{\odot,1_y}^{\Sigma}$. Therefore, $v_{0_y}^{\Sigma}$,
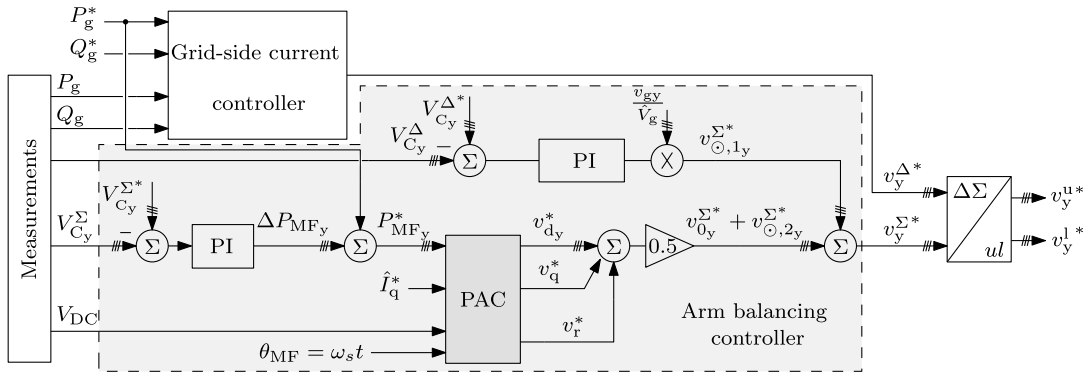
FIGURE 6. Integration of the PAC method in the control scheme of the MMC.

$v_{\odot,1_y}^{\Sigma}$, and $v_{\odot,2_y}^{\Sigma}$ are the three variables that are adjusted by the arm balancing controller.

B. INTEGRATION OF PAC

An arm balancing controller is developed here to integrate the PAC method and ensure an equal energy distribution between the arms. Fig. 6 shows the arm balancing controller that integrates the PAC method. The common-mode capacitor voltage of the leg $V_{C_y}^{\Sigma}$ is measured and then compared to the reference value $V_{C_y}^{\Sigma^*}$, which equals the sub-module capacitor reference voltage multiplied by the number of sub-modules in each arm according to (8). The result then is fed into a PI controller which generates a power error ΔP_{MF_y} to counteract the discrepancy in the common-mode capacitor voltage. To obtain a quick control action, the grid-power reference P_g^* is also added as a feed-forward term to the output of the PI controller to yield the MF power reference $P_{MF_y}^*$ for each MMC leg. These reference along with the required reactive current reference $\hat{I}_q^*$ are translated into $v_{d_y}^*$ and v_q^*, respectively. The reference for v_r is synthesized using the output dc voltage and modulation signal of the ac/dc converter. v_r^* and v_q^* are the same for all three legs, while $v_{d_y}^*$ can be different due to possible unequal discrepancies in the common-mode capacitor voltage $V_{C_y}^{\Sigma}$ of the legs. Hence, this control loop adjusts the power flow between the MMC and the LVC and the total energy mismatch between the MMC legs using $v_{0_y}^{\Sigma^*}$ and $v_{\odot,2_y}^{\Sigma^*}$, respectively.

The second control loop regulates the difference of the upper arm and lower arm capacitor voltages (differential-mode capacitor voltage $V_{C_y}^{\Delta}$) to zero. To this end, $V_{C_y}^{\Delta}$ is first compared with its setpoint $V_{C_y}^{\Delta^*}$, which is normally zero, and then fed into a PI controller. The output of the PI controller is multiplied by the corresponding normalized phase voltage, since $v_{\odot,1_y}^{\Sigma^*}$ must have a frequency equal to the grid voltage. Summing up the derived variables gives the references for the common-mode voltages. The references for the arm differential-mode voltages are generated by the grid-side current controller. The common- and differential-mode voltage setpoints $v_y^{\Sigma^*}$ and $v_y^{\Delta^*}$ are then transformed to upper and
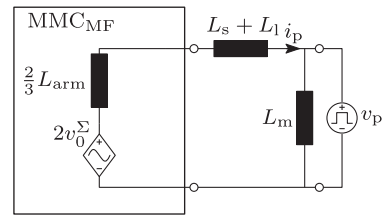
FIGURE 7. Rearranged MF terminal model.

lower arm voltage setpoints $v_y^{u^*}$ and $v_y^{l^*}$ which are fed to the PWM and sort-and-select algorithms.

Under balanced circuit parameters, the circulating terms are zero in steady-sate and are not present in the arm common-mode voltage v_y^{Σ}. Hence, the MF terminal model of the MMC, shown in Fig. 4(b), can be rearranged using Thevenin's theorem, as depicted in Fig. 7. In the rearranged MF terminal model, the voltage $2v_0^{\Sigma}$ is equivalent to v_{MF} (in Fig. 2(a)), which serves as a control parameter for adjusting the active and reactive power exchange between the MMC and the LVC.

IV. SIMULATION RESULTS

The converter is modeled and simulated in PLECS with the circuit parameters given in Table 1. The simulated converter uses an averaged model to model the MMC arms [3]. Fig. 8 illustrates the steady-state operation of the converter for power flow from an ac grid to a dc source. The phase voltage of the grid and the corresponding lower arm voltage is plotted, where the arm voltage is composed of the LF and MF voltage components. The MF voltage components are the same for all arms, while the LF components inverted for the upper arms, and shifted by 120° in-between the phase legs. The primary winding current is a trapezoidal current with a small reactive component to minimize both conduction and switching losses. This also decreases the peak-peak value of the dc-link current compared to phase-shift control [4], as shown in Fig. 8. The small negative current seen in the dc-link current corresponds to the switching current of power devices in the LVC.

TABLE 1. Simulated Circuit Specifications

	Parameter	Value
Grid		
Grid line-line voltage	$\sqrt{3}V_g$	25 kV
Grid frequency	f_g	50 Hz
MMC		
Equivalent capacitance of the arm	C_{sm}	1 mF
Arm inductance	L_{arm}	3 mH
MFT		
Turn ratio	n	10
Leakage inductance	L_l	500 µH
Magnetizing inductance	L_m	1 H
LVC		
Output dc voltage	V_{DC}	800 V
Switching frequency	f_s	1 kHz
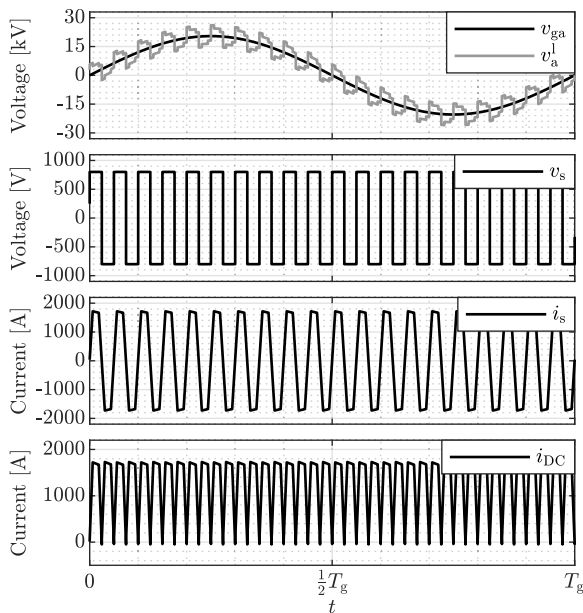
FIGURE 8. Simulated steady-state operation of the converter for power flow of $P_g^* = +1$ MW.

FIGURE 9. Transient waveforms with two possible strategies to update control variables: (a) updating V_d upon updating the power reference P_{MF}^* and (b) updating V_d at the middle of the first pulse upon updating the power reference P_{MF}^*.

FIGURE 10. Simulation results for a step change in the power reference P_g^* from -0.5 MW to -1 MW and some of the results in the zoomed time interval centered at $t = 0.2$ s.

Changing the control variables, such as V_d and δ, can results in imbalance of the volt-seconds applied to the magnetic components of the circuit. Left unchecked, these imbalances generate dc-bias currents and can impair the performance the arm inductors and the MFT which interconnect the MMC and the LVC. In phase-shift controlled converters, this problem is in principle inevitable, and requires dynamic changes in the control variables to suppress the volt-second imbalance [14]. Fig. 9 presents two possible strategies to update the control variable V_d upon a change in the power reference. In Fig. 9(a), the voltage V_d is updated directly, corresponding to the desired steady-state current. This causes the current i_d to rise above its desired level, res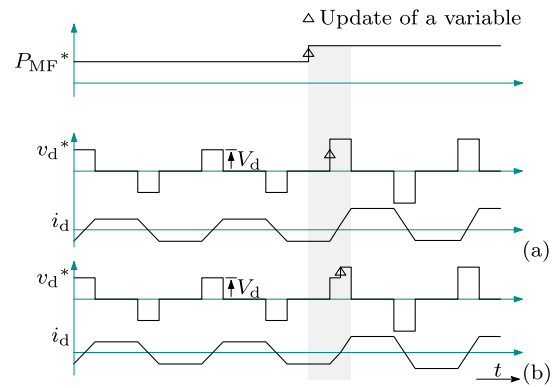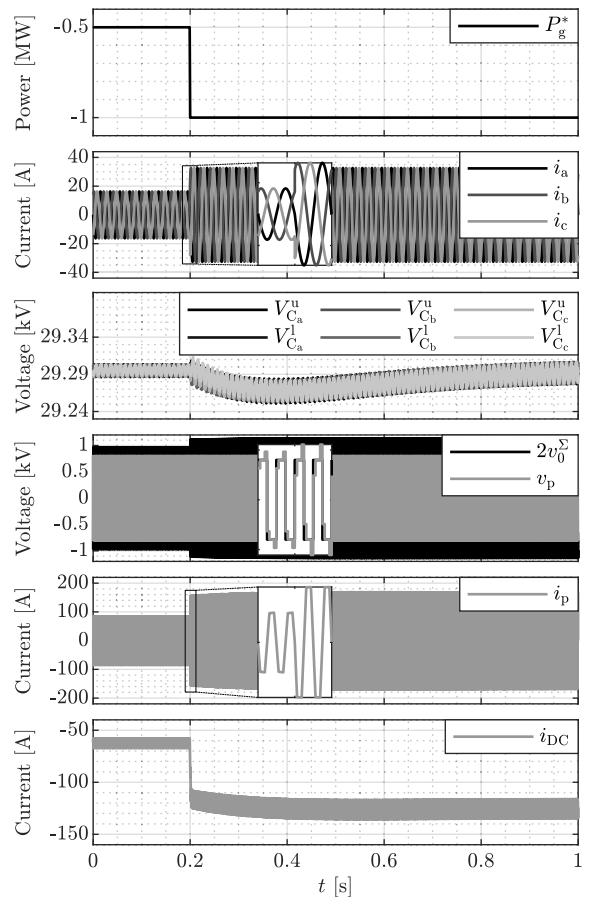ulting in a dc current component. As can be seen from Fig. 9(b), the proposed operating principle (PAC) can prevent the occurrence of imbalances by updating the control variable V_d at the zero crossing of i_d.

Fig. 10 shows the case of a power step from -0.5 MW to -1 MW. As can be seen, the average capacitor voltage of
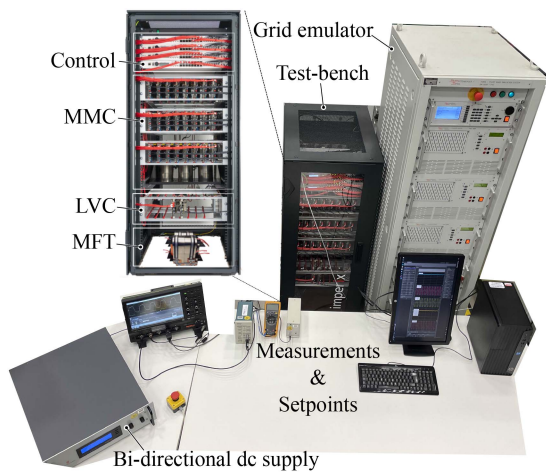
FIGURE 11. Test-bench of the MMC-based charger.

TABLE 2. Experimental Parameters

	Symbol	Value
MMC		
Grid line-line voltage	$\sqrt{3}V_g$	190 V
Number of sub-modules per arm	N_{sm}	4
Sub-module dc-link capacitance	C_{sm}	5 mF
Arm inductance	L_{arm}	2.3 mH
MFT		
Turn ratio	n	1
Leakage inductance	L_l	20 µH
Magnetizing inductance	L_m	17 mH
External series inductance	L_s	500 µH
LVC		
Output dc voltage	V_{DC}	300 V
Switching frequency	f_s	1 kHz

sub-modules are well-balanced during the step change in the power, and the dc-link current reaches its steady-state value in a few grid cycles. By virtue of the proposed strategy to update the control variables, no dc-bias currents are generated during the step change of the power.

V. EXPERIMENTAL VERIFICATION

The experimental results are obtained from the MMC-based ac/dc test-bench which is shown in Fig. 11. The test-bench comprises three main components: a modular multilevel converter, a medium frequency transformer, and a full-bridge ac/dc converter. The MMC consists of 24 sub-modules, with each arm consisting of 4 sub-modules (IMPERIX PEH2015). These sub-modules are implemented as full-bridge converters utilizing IGBT switches. The MFT constructed using Metglas AMCC (2605SA1) series cut cores, since this material suits the chosen operating frequency of the transformer. Furthermore, the ac/dc converter is realized as a full-bridge converter using two half bridges (IMPERIX PEB8038), which employ SiC MOSFETs. The circuit parameters of the prototype are given in Table 2. For both power-flow directions, the reactive power setpoint for the grid-side current controller is set to zero. The ac-terminal waveforms of the ac/dc converter are measured for both power directions.

Fig. 12 depicts the ac-link waveforms of the LVC for the power flow of ± 2000 W. To show that full soft-switching operation is obtained, the ac-link voltage and current within the switching transition are shown on the right hand side of Fig. 12. As can be seen from Fig. 12(a), for the positive direction of the power, the commutation current is large enough to fully charge or discharge the switch-node capacitance. The waveforms for the reverse power-flow direction are shown in Fig. 12(b), where the delivered power to the grid is set to 2000 W. By doing so the power losses of the MMC are compensated through the MF-side power, so that the amplitude of the current is larger compared to that of the positive power flow in Fig. 12(a). The ac-link voltage and current
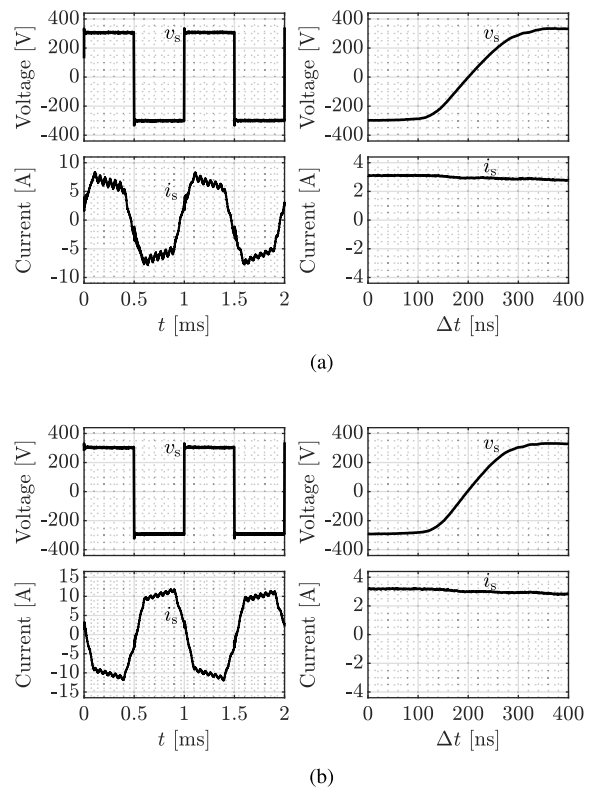

(a)

(b)

FIGURE 12. Measured ac-link waveforms of the LVC for the power flow of (a) +2000 W and (b) −2000 W and the results in the zoomed time interval centered at $t = 1$ ms (right).

waveforms within the switching transition confirms the full soft-switching operation of the ac/dc converter as shown on the right hand side of Fig. 12(b).

As discussed in the previous sections, the switching current I_{sw} can be controlled using the PAC method. The switching current, in turn, governs the charging and discharging of the
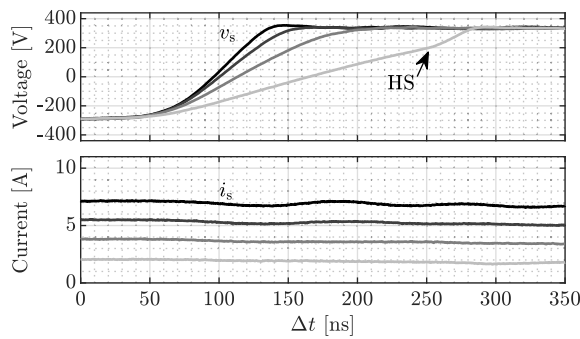
FIGURE 13. Measured ac-link voltage and current waveforms during the switching transition.
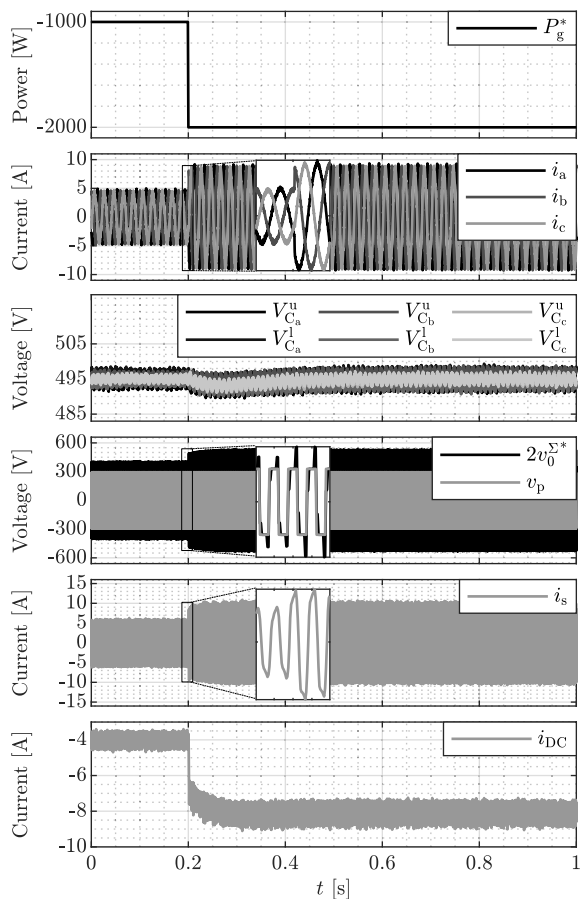

FIGURE 14. Measurement results for a step change in the power setpoint P_g^* from $-1000\,\text{W}$ to $-2000\,\text{W}$ and some of the results in the zoomed time interval centered at $t = 0.2\,\text{s}$.

switch-node capacitance. Fig. 13 shows the ac-link waveforms of the LVC during the switching transition for different switching currents. For the lowest value of I_{sw}, it can be seen from the voltage v_s that the switching current is not sufficient to have natural commutation of the switch-node voltage, and it experiences hard switching when the high-side switch is turned on. Although larger switching currents ensure ZVS turn-on of power switches, they increase the hard turn-off

losses of power devices in the LVC and dv/dt across the transformer windings. As a result, the switching current reference should be kept to the minimum required commutation current.

Fig. 14 shows the case of a power step from $-1000\,\text{W}$ to $-2000\,\text{W}$. As can be seen, the average capacitor voltage of sub-modules are well-balanced during the step change in the power, and the dc-link current reaches its steady-state value in a few grid cycles. During the step change of the power, there is an almost imperceptibly amount of dc-bias current, seen in Fig. 14, which is due to the inevitable timing mismatches in the PWM modulators and switching circuits.
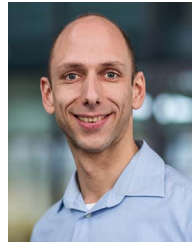
With the proposed operating principle, the LVC experiences lossless switching across the entire load range. Although analysis of the influence of the PAC method on the losses of the MMC is important to optimise the total losses of the converter, this paper does not delve into a comprehensive loss model for the MMC. Generally, conduction losses are the primary contributors to the MMC's total losses [15]. As demonstrated in [4], the PAC method offers a trade-off between the minimum number of sub-modules and RMS current stress in the MMC. Furthermore, any potential increase in the MMC's conduction losses can be offset by a significant reduction in the LVC's switching losses. It is important to note that this relationship is influenced by several factors in design and implementation of the system, such as the types of semiconductors in the MMC and LVC, the MMC's modulation scheme, and voltage and current levels, etc. While the example design discussed in this paper and [4] provides insights on how the proposed method affects the performance of the converter, it is not exhaustive and future work is still required.

VI. CONCLUSION

This paper presents a bi-directional MMC-based ultra-fast charger that consists of an MMC, a step-down medium frequency transformer, and a low-voltage ac/dc converter. A new operating principle has been proposed for the MMC-connected ac/dc converter. It uses three pulse-shaped voltage components to build the output voltage of the MMC. By doing so, a trapezoidal current with an adjustable reactive component is achieved in the MMC output, which maintains lossless switching of the power switches of the low voltage converter and minimizes the RMS currents in the converter. A dedicated control scheme that addresses the proposed operating principle and capacitor voltage balancing of the MMC has been developed. The developed control method successfully integrates the proposed operating principle while sustaining the total and internal energy balance of the MMC. It is also shown that, unlike typical phase-shift controlled converters, dc-bias currents can be readily avoided during the step change of the power. The validity and practical feasibility of the proposed operating principle and the developed control scheme have been verified by an MMC-based test-bench.

REFERENCES

[1] H. Tu, H. Feng, S. Srdic, and S. Lukic, "Extreme fast charging of electric vehicles: A technology overview," *IEEE Trans. Transp. Electrific.*, vol. 5, no. 4, pp. 861–878, Dec. 2019.

[2] F. Rojas, M. Díaz, M. Espinoza, and R. Cárdenas, "A solid state transformer based on a three-phase to single-phase modular multilevel converter for power distribution networks," in *Proc. IEEE Southern Power Electron. Conf.*, 2017, pp. 1–6.

[3] Y. P. Marca, M. G. L. Roes, J. L. Duarte, and K. G. E. Wijnands, "Isolated MMC-based AC/AC stage for ultrafast chargers," in *Proc. IEEE 30th Int. Symp. Ind. Electron.*, 2021, pp. 01–08.

[4] K. Pouresmaeil, J. Duarte, K. Wijnands, M. Roes, and N. Baars, "Single-phase bidirectional ZVZCS AC-DC converter for MV-connected ultra-fast chargers," in *Proc. IEEE PCIM Europe; Int. Exhib. Conf. Power Electron., Intell. Motion, Renewable Energy Manage.*, 2022, pp. 1–7.

[5] R. Agarwal, S. Martin, Y. Shi, and H. Li, "High frequency transformer core loss analysis in isolated modular multilevel DC-DC converter for MVDC application," in *Proc. IEEE Energy Convers. Congr. Expo.*, 2019, pp. 6419–6423.

[6] M. Glinka and R. Marquardt, "A new AC/AC-multilevel converter family applied to a single-phase converter," in *Proc. IEEE 5th Int. Conf. Power Electron. Drive Syst.*, 2003, pp. 16–23.

[7] S. Kenzelmann, A. Rufer, D. Dujic, F. Canales, and Y. R. de Novaes, "Isolated DC/DC structure based on modular multilevel converter," *IEEE Trans. Power Electron.*, vol. 30, no. 1, pp. 89–98, Jan. 2015.

[8] S. Zhao, Y. Chen, S. Cui, B. J. Mortimer, and R. W. De Doncker, "Three-port bidirectional operation scheme of modular-multilevel DC–DC converters interconnecting MVDC and LVDC grids," *IEEE Trans. Power Electron.*, vol. 36, no. 7, pp. 7342–7348, Jul. 2021.

[9] T. Ohta, P.-Y. Huang, and Y. Kado, "Bidirectional isolated ripple cancel triple active bridge DC-DC converter," in *Proc. IEEE 22nd Eur. Conf. Power Electron. Appl.*, 2020, pp. P.1–P.9.

[10] S. Cui, J. Hu, and R. W. De Doncker, "Control and experiment of a TLC-MMC hybrid DC–DC converter for the interconnection of MVDC and HVDC grids," *IEEE Trans. Power Electron.*, vol. 35, no. 3, pp. 2353–2362, Mar. 2020.

[11] M. Schnarrenberger, F. Kammerer, M. Gommeringer, J. Kolb, and M. Braun, "Current control and energy balancing of a square-wave powered 1AC-3AC modular multilevel converter," in *Proc. IEEE Energy Convers. Congr. Expo.*, 2015, pp. 3607–3614.

[12] R. Haneda and H. Akagi, "Design and performance of the 850-V100-kW 16-kHz bidirectional isolated DC–DC converter using SiC-MOSFET/SBD H-bridge modules," *IEEE Trans. Power Electron.*, vol. 35, no. 10, pp. 10013–10025, Oct. 2020.

[13] S. Milovanović and D. Dujić, "Comprehensive comparison of modular multilevel converter internal energy balancing methods," *IEEE Trans. Power Electron.*, vol. 36, no. 8, pp. 8962–8977, Aug. 2021.

[14] J. Hu, S. Cui, D.V.d. Hoff, and R. W. De Doncker, "Generic dynamic phase-shift control for bidirectional dual-active bridge converters," *IEEE Trans. Power Electron.*, vol. 36, no. 6, pp. 6197–6202, Jun. 2021.

[15] M. Glinka, *Modulares Mehrpunkt-Umrichtersystem–ein neuartiges Konzept am Beispiel der elektrischen Traktion (Forschungsberichte Leistungselektronik und Steuerungen Series)*, vol. 4. Aachen, Germany: Shaker Verlag, 2011.

KAVEH POURESMAEIL (Graduate Student Member, IEEE) received the B.Sc. degree in electrical engineering from the University of Tabriz, Tabriz, Iran, in 2016, and the M.Sc. degree in power electronics from the Sharif University of Technology, Tehran, Iran, in 2018. Since 2021, he has been working toward the Ph.D. degree with the Electromechanics and Power Electronics (EPE) Group, Eindhoven University of Technology, Eindhoven, The Netherlands. His research focuses on high-power converters for charging infrastructure of electrified transportation.

MAURICE G.L. ROES (Member, IEEE) received the B.Sc. and M.Sc. degrees in electrical engineering from the Eindhoven University of Technology (TU/e), Eindhoven, The Netherlands, in 2005 and 2009, respectively, and the Ph.D. degree in electrical engineering from the Electromechanics and Power Electronics Group, Eindhoven University of Technology. After receiving the Ph.D. degree, he was a Researcher with the Electromechanics and Power Electronics Group, Eindhoven University of Technology, and in 2016, he was appointed Assistant Professor there. His research interests include advanced (digital) control of power converters, modern control theory, state estimation, and modeling of Multiphysics systems.

NICO H. BAARS received the B.Eng. degree in electrical engineering from the HAN University of Applied Sciences, Arnhem, The Netherlands, the M.Sc. degree and Ph.D. degree (*cum laude*) in electrical engineering from the Eindhoven University of Technology, Eindhoven, The Netherlands, in 2013 and 2017, respectively. After receiving the Ph.D. degree, he started working with Strukton Power where he is responsible for power converters for rolling stock and railway power supply applications. Since 2017, he has been a visiting Researcher with Electromechanics and Power Electronics Group, Eindhoven University of Technology. His research interests include soft-switching and modulation strategies in power converters.

CORNELIS G.E. WIJNANDS received the M.Sc. degree in electrical engineering from the Eindhoven University of Technology, Eindhoven, The Netherlands, in 1994. In 1994, he joined Prodrive Technologies B.V., where he started to work on the development of power electronics and control. He is currently a Senior Electronics Architect with Prodrive Technologies B.V., Son, The Netherlands. In 2009, he became a part-time Assistant Professor with the Electromechanics and Power Electronics group, Eindhoven University of Technology, where he has been a Full Professor since 2017. He is currently a part-time Professor with the Electrical Energy Systems group, Eindhoven University of Technology. His research interests include high precision amplifiers and smart grid electronics.